Rapid detachment of a rigid sphere adhered to a viscoelastic substrate: An upper bound model incorporating Maugis parameter and preload effects

Qingao Wang [a], Antonio Papangelo [c,d], Michele Ciavarella [c,d], Huajian Gao [b], Qunyang Li [a,b,*]

[a] *AML, Department of Engineering Mechanics, Tsinghua University, Beijing 100084, China*
[b] *Mechano-X Institute, Tsinghua University, Beijing 100084, China*
[c] *Department of Mechanics, Mathematics and Management, Politecnico di Bari, via Orabona 4, Bari, 70125, Italy*
[d] *Department of Mechanical Engineering, Hamburg University of Technology, Am Schwarzenberg-Campus 1, Hamburg, 21073, Germany*

ARTICLE INFO

ABSTRACT

For a typical adhesive contact problem, a rigid sphere initially adhered to a relaxed viscoelastic substrate is pulled away from the substrate at finite speeds, and the pull-off force is often found to depend on the rate of pulling. Despite significant theoretical advancements in this area, how the apparent adhesion enhancement is affected by the Maugis parameter and preload remains unclear, and existing models are sometimes contentious. In this work, we revisit this adhesive contact problem and propose a theoretical model to predict the upper bound detachment behavior when the pulling speed approaches infinity. Our analysis reveals that the apparent work of adhesion can always be enhanced, regardless of the Maugis parameter, when the initial contact radius exceeds a critical threshold. Conversely, when the initial contact radius is below this critical value, the adhesion enhancement becomes limited and depends on both the Maugis parameter and the preload condition. Further model calculations suggest that the critical initial contact radius is dependent on the Maugis parameter. In the JKR-like regime, this critical radius converges to a constant value, whereas in the DMT-like regime, it diverges rapidly following an inverse power law with respect to the Maugis parameter. As a result, observing adhesion enhancement is generally more challenging in DMT-like contacts compared to JKR-like contacts. In the meantime, our model also suggests that the adhesion enhancement arises from the expansion of the cohesive zone area due to the viscoelastic properties of the material not only within the cohesive zone but also in the intimate contact zone. Overall, our findings offer a more comprehensive understanding of viscoelastic effects in adhesive contacts, which can be used to rationally predict or optimize adhesion strength in viscoelastic interfaces.

1. Introduction

Adhesion is ubiquitous in both natural and engineering systems, and the strength of adhered interfaces is often critical for their functionality and integrity (Kendall, 2001). The strength of an adhered interface is typically measured by the maximum tensile force

---

* Corresponding author.
E-mail address: qunyang@tsinghua.edu.cn (Q. Li).

required to separate the joint, known as the pull-off force. For two elastic bodies with axisymmetric profiles interacting through an adhesive interface, several theoretical models have been developed to describe their mechanical behavior. Assuming that the adhesive forces are only present within the contact area, the Johnson-Kendall-Roberts (JKR) model (Johnson et al., 1971) predicts the pull-off force to be $P_{JKR} = 1.5\pi Rw$, where R is the equivalent radius of curvature (which depends on the radii of curvature of two contacting bodies as in Hertz theory) and w is the work of adhesion. In contrast, adopting a Hertzian type contact profile and taking account of the additional attractive interactions outside the area of contact, the Derjaguin-Muller-Toporov (DMT) model (Derjaguin et al., 1975) predicts the pull-off force to be $P_{DMT} = 2\pi Rw$. These two seemingly contradicting models were later found to be able to transit from one to the other by introducing a non-dimensional parameter $\mu = \left[Rw^2 / \left(E^{*2} h_0^3 \right) \right]^{1/3}$, where E^* is the effective plane strain elastic modulus and h_0 is the equilibrium distance of the adhesive interactions (Tabor, 1976). For stiff solids with small radii and low adhesion energies ($\mu \ll 1$), the DMT model is applicable. In contrast, for soft solids with large radii and high adhesion energies ($\mu \gg 1$), the JKR theory is more appropriate. The transition from the DMT regime to the JKR regime was also examined by Maugis by adopting a Dugdale cohesive zone model (Maugis, 1992), where the system behavior is controlled by a non-dimensional parameter similar to the Tabor parameter, $\lambda = 2\sigma_0 / \left(\pi w \chi^2 / R \right)^{1/3}$, where $\chi = 4E^*/3$ and σ_0 denotes the adhesive strength. For all these classical theories, the pull-off force of an axisymmetric adhesive contact system would range from $1.5\pi Rw$ to $2\pi Rw$, exhibiting only weak dependence on the elasticity of the contacting bodies.

In contrast to the quasi-static theories, the strength of adhered interfaces is often found to be significantly influenced by the pulling speed in the experiments, especially when viscoelastic materials are involved. Typically, one observes stronger apparent interface adhesion when the pulling speed is faster (Chen et al., 2013; Das and Chasiotis, 2021; Feng et al., 2007; Liang et al., 2020; Lorenz et al., 2013; Maghami et al., 2024b; Meitl et al., 2006; Peng et al., 2014; Petroli et al., 2022; Vandonselaar et al., 2023; Violano et al., 2021b; Yin et al., 2024). Early study on the rate effect of the interface adhesion can be traced back to a series of peeling experiments in the 1970s, where the apparent work of adhesion was found to be enhanced with increasing peeling speeds (Gent and Schultz, 1972; Maugis and Barquins, 1978). Such speed dependence is commonly described by the empirical Gent-Schultz law, $w_{app}(v_c) = w[1 + \beta(a_T v_c)^n]$, where w is the intrinsic work of adhesion, v_c is the velocity of the interfacial crack, a_T is Williams-Landel-Ferry shift factor (Williams et al., 1955), β and n are material parameters. Owing to its simplicity, the Gent-Schultz law has been widely used in analyzing the viscoelastic adhesive contact problems by simply replacing the work of adhesion w with the apparent work of adhesion w_{app}(Ciavarella, 2021; Muller, 1999; Violano et al., 2021a; Wang and Liu, 2024). Despite the success in capturing the rate dependence, the phenomenological models fall short in providing an physical explanation, and their applicability is typically limited to the experimental data available for fitting (Lorenz et al., 2013; Peng et al., 2014; Petroli et al., 2022; Violano et al., 2021b, c).

Because the decohesion process of an adhesive interface involves propagation of the interfacial crack, the rate dependent adhesion behavior can be understood in the context of viscoelastic fracture mechanics. For a semi-infinite crack growing steadily in an infinite linear viscoelastic solid, Knauss (1973) formulated an expression for the crack opening displacement based on a left-trapezoid cohesive zone model and established a relationship between the apparent fracture toughness and the crack propagation speed. Schapery revisited this problem in a series of papers (Schapery, 1975a, b, c), where he introduced the concept of effective compliance and derived an approximate yet analytical expression for the apparent fracture toughness. Later, a numerical but exact solution was proposed by Greenwood (2004) based on the classic three-element viscoelastic solids and the Dugdale cohesive zone model. Besides the cohesive zone model approach, viscoelastic fracture can also be examined from an energy balance perspective. By considering equilibrium between the work by the applied load and the bulk dissipation due to viscoelasticity and the energy related to the creation of new surfaces, de Gennes obtained a dissipation scaling law semi-qualitatively (de Gennes, 1996). This scheme was further developed by Persson and Brener, who derived an analytical expression for the apparent fracture toughness as a function of crack propagation speed by assuming a linear elastic K-field (Persson and Brener, 2005). Although the energy based models seem different from the cohesive zone models, it has been found that these two types of approaches can give consistent results if the size of the cut-off radius adopted in the Persson-Brener theory is properly chosen (Afferrante and Violano, 2022; Ciavarella et al., 2021; Hui et al., 2022; Persson, 2021). Furthermore, both types of theories predict that the apparent fracture toughness at very high crack speeds Γ_{app}^∞ would be amplified to a value that is determined by the ratio between the instantaneous and relaxed moduli of the viscoelastic materials, *i.e.* $\Gamma_{app}^\infty / \Gamma_0 = E_I / E_R$ where Γ_0 is the intrinsic fracture toughness. This theoretical amplification factor is valid for semi-infinite cracks, but finite size effects may strongly reduce it even considering infinite crack speed (Maghami et al., 2024a).

The relationship between the apparent fracture toughness and the crack propagation speed can be extended to explain the rate effect in the viscoelastic adhesion. Greenwood and Johnson examined the rate-dependent adhesion between a viscoelastic sphere and a rigid plane based on the fracture mechanics approach (Greenwood and Johnson, 1981). Specifically, by invoking Schapery's effective compliance to calculate the crack opening displacement, they attributed the enhanced adhesion at high loading rates to the extension of the cohesive zone. Later, Johnson and coworkers (Johnson, 1999; Johnson and Greenwood, 2002) worked out the apparent work of adhesion w_{app} for opening and closing interfacial cracks under a constant loading rate, where they found that the maximum enhancement for the pull-off force could be up to a factor of (E_I / E_R). In their derivations, the bulk material exhibits a relaxed modulus, while the material around the cohesive zone is deformed with an instantaneous modulus. Such treatment is based on the implicit assumption that the cohesive zone size is much smaller than the contact radius, placing it withinthe JKR-like regime. However, using finite element method (FEM) simulations, Lin and Hui showed that such assumption might break down even in the JKR-like regime if the loading rate is fast enough such that the bulk deformation rate is comparable to the viscoelastic relaxation rate (Lin and Hui, 2002). Barthel and coworkers have also developed theories for viscoelastic adhesion problems by considering either the JKR-like regime (Barthel, 2008; Barthel and Haiat, 2002) or a more general contact configuration (Haiat et al., 2003). However, their derivations are

mathematically complex, which significantly limits their applications.

Recently, Das and Chasiotis revisited the contact problem of a rigid sphere being retracted from a fully relaxed viscoelastic substrate at a finite speed by extending the Maugis-Dugdale model with an apparent work of adhesion (Das and Chasiotis, 2021). They found that the pull-off force would monotonically increase with the retraction rate and saturate at an amplification factor of (E_I /E_R) at an infinite speed. Moreover, their model predicts that the adhesion enhancement is independent of the initial contact radius a_0 and the Maugis parameter λ. In contrast to the Das-Chasiotis approach, Ciavarella used the Schapery effective compliance to incorporate the viscoelastic effect in the Maugis-Dugdale model (Ciavarella, 2022; Ciavarella et al., 2023). The model calculations by Ciavarella show that increasing the loading rate does not necessarily lead to stronger apparent adhesion; instead, the adhesion enhancement is dependent on the Maugis parameter. In the JKR-like regime ($\lambda > 100$), the pull-off force increases monotonically with the loading rate, eventually reaching a plateau at an amplification factor of (E_I /E_R). However, in the DMT-like regime ($\lambda < 0.1$), increasing the loading rate does not enhance the pull-off force. The lack of adhesion enhancement in the DMT-like regime is qualitatively consistent with the FEM simulations by Violano and Afferrante (2022a), where the loading rate was found to have little effect on the pull-off force for systems with long-range adhesive interactions. However, in the FEM simulations (Jiang et al., 2021; Violano and Afferrante, 2022b) and boundary element method (BEM) simulations (Maghami et al., 2024b), the enhanced pull-off force in cases of short- or mid-range adhesive interactions can be significantly affected by the initial contact radius, which is not captured by the existing theoretical predictions (Ciavarella, 2022; Ciavarella et al., 2023; Das and Chasiotis, 2021).

In summary, for the typical viscoelastic adhesive contact problem, where an indenter initially adhered to a fully relaxed viscoelastic substrate is then retracted at finite speeds, two fundamental questions remain unresolved despite the extensive studies. First, how does the enhancement of the apparent adhesion depend on the Maugis parameter? Should we expect an enhanced apparent adhesion at high loading rates in the DMT-like regime? Second, for those cases showing enhanced apparent adhesion, how does the adhesion enhancement depend on the preload? To address these questions, we will revisit the detachment behavior of the aforementioned system. To make the problem more tractable while still being able to address the above key questions, we will focus on an upper bound analysis in the present paper, examining the detachment behaviors when the retracting speed is infinitely large. The cases involving finite loading speeds will be discussed in a separate paper later. In this work, we will first propose a theoretical model to describe the rate-dependent detachment behavior based on the Barthel framework (Haiat et al., 2003) and Maugis-Dugdale contact configuration (Maugis, 1992). We will then examine the dependence of the apparent work of adhesion on the Maugis parameter and preload conditions, followed by a discussion of our findings in the context of existing predictions in literature. Finally, our model predictions will be validated through boundary element method (BEM) simulations.
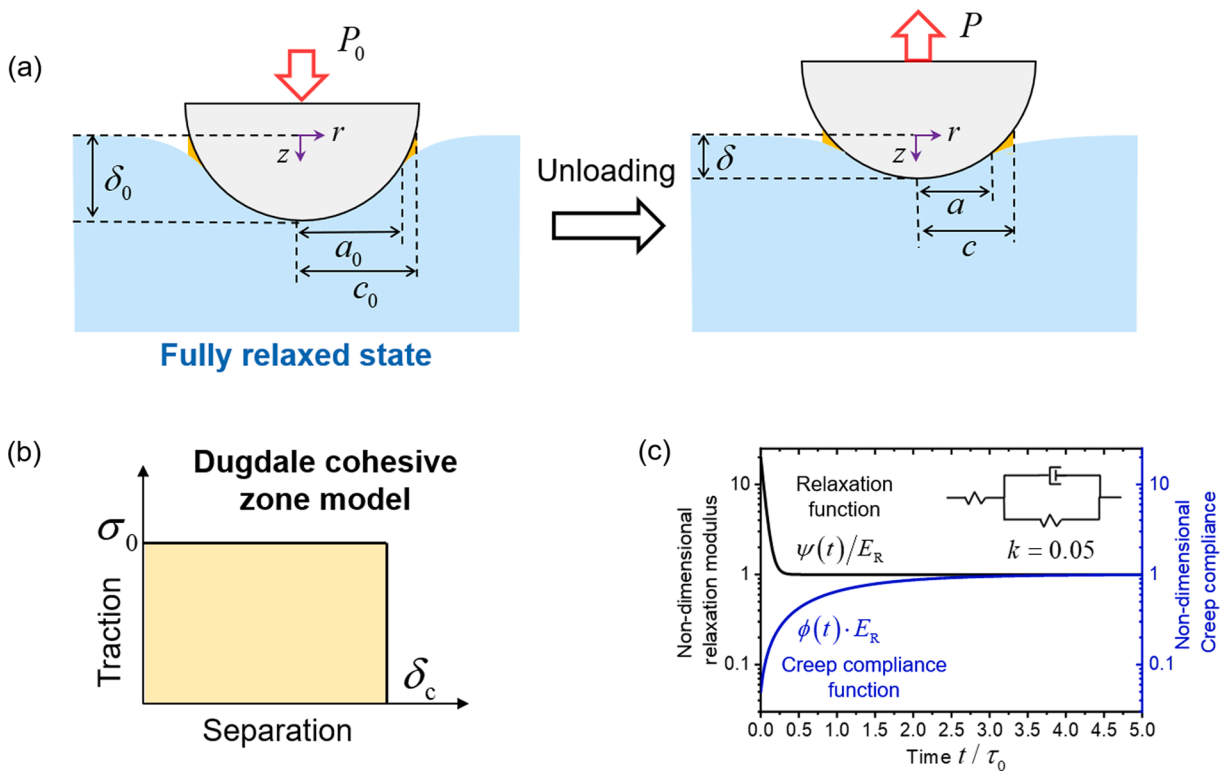

Fig. 1. (a) Model Setup: a rigid sphere, initially compressed to adhere to a fully relaxed viscoelastic substrate, is then retracted at an infinite speed. (b) The separation-traction law of the Dugdale-type cohesive zone model. (c) Typical relaxation and creep functions with $k = 0.05$.

2. Theoretical model

In this work, we consider the adhesive contact problem between a rigid sphere and a viscoelastic substrate. As depicted in Fig. 1 (a), a rigid sphere of radius R is first slowly pressed into a viscoelastic substrate under a normal force P_0, resulting in an initial contact radius a_0, an outer radius of the cohesive zone c_0, and an indentation displacement δ_0. The sphere is then retracted from this relaxed viscoelastic substrate at an infinite speed until full detachment. It is assumed that the contact interface is frictionless and the adhesive interactions can be described by the Dugdale cohesive zone model where a constant traction σ_0 exists within a critical distance δ_c, as shown in Fig. 1 (b). In our model, the viscoelastic substrate is assumed to be linear viscoelastic and the stress-strain relations can be determined as follows:

$$\sigma(t) = \int_{-\infty}^{t} d\tau \cdot \psi(t - \tau) \frac{d\varepsilon(\tau)}{d\tau}, \tag{1}$$

and

$$\varepsilon(t) = \int_{-\infty}^{t} d\tau \cdot \phi(t - \tau) \frac{d\sigma(\tau)}{d\tau}, \tag{2}$$

where $\psi(t)$ is the relaxation function and $\phi(t)$ is the creep compliance function. Similar to the previous studies (Afferrante and Violano, 2022; Ciavarella, 2022; Greenwood and Johnson, 1981; Violano and Afferrante, 2022a), a three-element standard linear solid is adopted for the viscoelastic substrate. The relaxation function and creep compliance function are

$$\psi(t) = E_R \left[1 + \left(\frac{1 - k}{k} \right) \exp \left(-\frac{t}{k \tau_0} \right) \right], \tag{3}$$

and

$$\phi(t) = \frac{1}{E_R} \left[1 - (1 - k) \exp \left(-\frac{t}{\tau_0} \right) \right], \tag{4}$$

where E_R is the relaxed modulus, k is the relaxed-to-instantaneous modulus ratio and τ_0 is the characteristic relaxation time. The typical relaxation and creep curves for a three-element standard linear viscoelastic solid are schematically shown in Fig. 1 (c).

The formulation of our model is based on the framework proposed by Barthel and his coworkers (Haiat et al., 2003). For axisymmetric contact problems, two auxiliary functions of the Abel type integral transforms can be defined as:

$$g(r) = \int_{r}^{\infty} ds \cdot \frac{-s\sigma(s)}{\sqrt{s^2 - r^2}}, s > r, \tag{5}$$

and

$$\theta(r) = \frac{d}{dr} \int_{0}^{r} ds \cdot \frac{su(s)}{\sqrt{r^2 - s^2}}, s < r, \tag{6}$$

where $\sigma(r)$ is the normal stress along the contact interface (positive values represent tensile stress), and $u(r)$ the surface displacement in the normal direction (positive values indicate downward). The inverse of the above two auxiliary functions are:

$$\sigma(r) = \frac{2}{\pi} \int_{r}^{\infty} ds \cdot \frac{g'(s)}{\sqrt{s^2 - r^2}}, s > r, \tag{7}$$

and

$$u(r) = \frac{2}{\pi} \int_{0}^{r} ds \cdot \frac{\theta(s)}{\sqrt{r^2 - s^2}}, s < r. \tag{8}$$

For the viscoelastic problem considered in this work, the relationship between the two auxiliary functions are

$$g(r, t) = K_R \int_{-\infty}^{t} d\tau \cdot \overline{\psi}(t - \tau) \frac{\partial}{\partial \tau} \theta(r, \tau), \tag{9}$$

and

$$\theta(r, t) = \frac{1}{K_R} \int_{-\infty}^{t} d\tau \cdot \overline{\phi}(t - \tau) \frac{\partial}{\partial \tau} g(r, \tau), \tag{10}$$

where $K_R = E_R^*/2$, $E_R^* = E_R/(1 - \nu^2)$ is the plane strain modulus, ν is the Poisson's ratio and $\overline{\psi}(t) = \psi(t)/E_R^*$ and $\overline{\phi}(t) = \phi(t) \cdot E_R^*$ are the non-dimensional relaxation and creep compliance functions, respectively. Given that the initial state is fully relaxed, we have $g_0(r) = K_R \theta_0(r)$, where $g_0(r)$ and $\theta_0(r)$ are the auxiliary functions at $t = 0$, *i.e.* the moment right before the retraction starts. Then, during the

retraction process, Eqs. (9) and (10) can be written as

$$g(r,t) = g_0(r) + K_R \int_0^t d\tau \cdot \overline{\psi}(t-\tau) \frac{\partial}{\partial \tau} \theta(r,\tau),$$ (11)

and

$$\theta(r,t) = \theta_0(r) + \frac{1}{K_R} \int_0^t d\tau \cdot \overline{\phi}(t-\tau) \frac{\partial}{\partial \tau} g(r,\tau).$$ (12)

The governing equations for the system can be derived by considering the following conditions:

2.1. Continuity of the auxiliary functions

At any time t during the detachment process, the corresponding indentation depth is denoted by δ, the contact radius is a and the outer radius of the cohesive zone is c. Within the contact zone, the surface of the substrate is deformed to match the profile of the indenter. Therefore, the displacement $u(r)$ can be determined as

$$u(r) = \delta - \frac{r^2}{2R}, 0 \leq r \leq a.$$ (13)

Here, we approximated the shape of the sphere using a parabola by assuming $a \ll R$. Following Eq. (6), the function of θ is determined to be

$$\theta(r) = \delta - \frac{r^2}{R}, 0 \leq r \leq a.$$ (14)

Considering the upper bound behavior associated with a rapid detachment, we set $t \to 0$. In this case, Eq. (11) is simplified as

$$g(r) = g_0(r) + \frac{K_R}{k} [\theta(r) - \theta_0(r)], 0 \leq r \leq a,$$ (15)

where $\theta_0(r) = \delta_0 - r^2/R$ and $g_0(r) = K_R \theta_0(r)$. Meanwhile, since the interfacial stress has a constant value σ_0 within the cohesive zone, the function g can be obtained from Eq. (5) as

$$g(r) = -\sigma_0 \sqrt{c^2 - r^2}, a \leq r \leq c.$$ (16)

Considering the continuity of g at $r = a$, we can obtain the first governing equation from Eqs. (15) and (16) as

$$\delta + (k-1)\delta_0 = \frac{ka^2}{R} - \frac{k\sigma_0}{K_R} \sqrt{c^2 - a^2}.$$ (17)

2.2. Balance of the forces

Considering the force balance of the sphere, we have

$$P + \int_0^c dr \cdot 2\pi r \sigma(r) = 0,$$ (18)

where P is the normal force (positive values correspond to compression, while negative means tension) and $\sigma(r)$ is the interfacial stress. Invoking the function of g, one gets

$$P = 4 \int_0^c dr \cdot g(r).$$ (19)

Substituting Eqs. (15) and (16) into Eq. (19), we obtain

$$P = \frac{4K_R a}{k} [\delta + (k-1)\delta_0] - \frac{4K_R}{3} \frac{a^3}{R} - 2\sigma_0 a^2 \left(m^2 \cdot \arctan\sqrt{m^2 - 1} - \sqrt{m^2 - 1} \right),$$ (20)

where $m = c/a$.

2.3. Critical opening displacement at the edge of the cohesive zone

As the sphere detaches from the substrate, both the contact zone and the cohesive zone contract towards the center of the contact. Particularly, the gap between the upper and lower surfaces of the interface at the outer edge of the cohesive zone remains at the critical value of δ_c, *i.e.*

$$h(c) = \delta_c,$$ (21)

where h is the interfacial gap. For the Dugdale-type cohesive zone, the critical gap for imminent separation can be expressed as $\delta_c = w/\sigma_0$. Considering the geometry of the sphere and the surface displacement, one can calculate the interfacial gap as

$$h(c) = -\delta + \frac{c^2}{2R} + u(c), \tag{22}$$

where $u(c)$ is the surface displacement at $r = c$. According to the inverse of θ function, $u(c)$ can be determined from

$$u(c) = \frac{2}{\pi} \int_0^c ds \cdot \frac{\theta(s)}{\sqrt{c^2 - s^2}}. \tag{23}$$

Since the expression of θ function in the contact zone $0 \leq s \leq a$ is given by Eq. (14), Eq. (23) can be rewritten as

$$u(c) = \frac{2}{\pi} \left[\delta \arcsin \frac{a}{c} - \frac{1}{2R} \left(c^2 \arcsin \frac{a}{c} - a\sqrt{c^2 - a^2} \right) \right] + \frac{2}{\pi} \int_a^c ds \cdot \frac{\theta(s)}{\sqrt{c^2 - s^2}}. \tag{24}$$

Substituting Eq. (24) into Eq. (22) yields

$$h(c) = \frac{2}{\pi R} \left[\frac{a}{2} \sqrt{c^2 - a^2} + \left(\frac{c^2}{2} - a^2 \right) \arctan \sqrt{m^2 - 1} \right] - \frac{2}{\pi} \left(\delta - \frac{a^2}{R} \right) \arctan \sqrt{m^2 - 1} + \frac{2}{\pi} \int_a^c ds \cdot \frac{\theta(s)}{\sqrt{c^2 - s^2}}. \tag{25}$$

Calculation of the last term on the right-hand side of Eq. (25) needs the expression of $\theta(s)$ in the cohesive zone $a \leq s \leq c$. Due to the viscoelastic nature, $\theta(s)$ will depend on the loading history of the system, which requires a detailed examination on the interfacial debonding process. As illustrated in Fig. 2, starting from the initial state $(a = a_0, c = c_0)$, both a and c begin to decrease as the sphere is retracted from the substrate. During the early stage, referred to as Stage-I, c remains larger than a_0 and the cohesive zone can be divided into two regions: $a \leq s \leq a_0$ and $a_0 \leq s \leq c$.

In the region $a_0 \leq s \leq c$, the upper and lower surfaces are continuously separated with a constant adhesive stress σ_0. Because the stress is known, one can calculate g function in this region using Eq. (16) and then covert it to θ function using Eq. (12). It is noted that, for the upper bound limit with an infinite retraction speed, Eq. (12) can be further simplified to

$$\theta(r) = \theta_0(r) + \frac{k}{K_R} \left[g(r) - g_0(r) \right]. \tag{26}$$

Therefore, substituting Eq. (16) into Eq. (26), we obtain $\theta(s)$ in the region $a_0 \leq s \leq c$ as

$$\theta(s) = \frac{k}{K_R} g(s) + \frac{1-k}{K_R} g_0(s), a_0 \leq s \leq c, \tag{27}$$

where $g_0(r) = -\sigma_0 \sqrt{c_0^2 - r^2}$.

In the region $a \leq s \leq a_0$, the loading history of the interface is more complicated. Initially, the interface lies within the contact area. As detachment begins, the upper and lower surfaces become separated and enter the cohesive zone. Similar to the region $a_0 \leq s \leq c$, g function in this region can be obtained from Eq. (16). According to the Eq. (26), we can also determine the θ function in this region. Therefore, $\theta(s)$ is determined as follows

$$\theta(s) = \frac{k}{K_R} g(s) + (1-k)\theta_0(s), a \leq s \leq a_0, \tag{28}$$
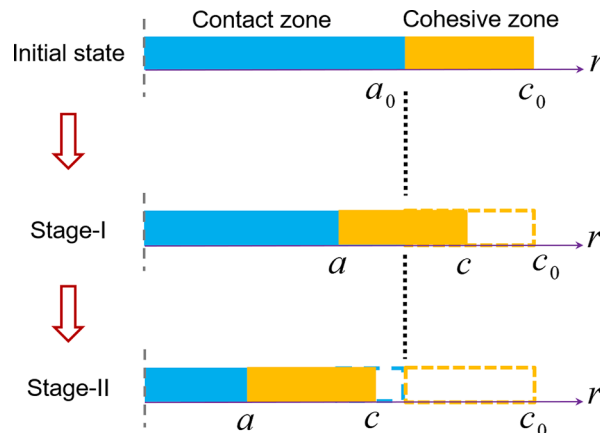

Fig. 2. A schematic diagram showing the evolution of the contact and cohesive zones during the interfacial crack propagation.

where $\theta_0(r) = \delta_0 - r^2/R$. It is worth mentioning that reducing Eq. (12) to Eq. (26) is only applicable for the upper bound limit when the retraction speed is infinitely large. If the retraction rate is finite, the treatment is much more complicated, which will be addressed separately in a future paper.

Therefore, by invoking Eqs. (27), (28) and (25), the critical gap condition at the edge of the cohesive zone for Stage-I becomes

$$
\begin{aligned}
&\frac{2}{\pi R}\left[\frac{a}{2}\sqrt{c^2-a^2}+\left(\frac{c^2}{2}-a^2\right)\arctan\sqrt{m^2-1}\right]-\frac{2}{\pi}\left(\delta-\frac{a^2}{R}\right)\arctan\sqrt{m^2-1}+\frac{2}{\pi}\frac{\sigma_0}{K_R}k(a-c)\\
&+\frac{2}{\pi R}(1-k)\left[\left(\delta_0-\frac{c^2}{2}\right)\left(\arcsin\frac{a_0}{c}-\arcsin\frac{a}{c}\right)\right]+\frac{2}{\pi R}(1-k)\left(\frac{1}{2}a_0\sqrt{c^2-a_0^2}-\frac{1}{2}a\sqrt{c^2-a^2}\right)\\
&+\frac{2}{\pi}\frac{\sigma_0}{K_R}(k-1)c_0\left[\mathrm{EllipticE}\left(\frac{\pi}{2},\frac{c^2}{c_0^2}\right)-\mathrm{EllipticE}\left(\arcsin\frac{a_0}{c},\frac{c^2}{c_0^2}\right)\right]\\
&=\frac{w}{\sigma_0}
\end{aligned}
\tag{29}
$$

where $\mathrm{EllipticE}(\alpha,p) = \int_0^\alpha dx \cdot \sqrt{1-p\sin^2 x}$ is the elliptic integral of the second kind. A more detailed derivation of Eq. (29) can be found in Appendix A.

As the retraction proceeds, a and c continue to decrease, entering a second stage where $c \le a_0$ (referred to as Stage-II). As illustrated in Fig. 2, the whole cohesive zone initially lies within the contact zone in Stage-II. Therefore, the corresponding $\theta(s)$ is determined by Eq. (28), and the governing equation at this stage becomes

$$
\begin{aligned}
&\frac{2}{\pi R}\left[\frac{a}{2}\sqrt{c^2-a^2}+\left(\frac{c^2}{2}-a^2\right)\arctan\sqrt{m^2-1}\right]-\frac{2}{\pi}\left(\delta-\frac{a^2}{R}\right)\arctan\sqrt{m^2-1}+\frac{2}{\pi}\frac{\sigma_0}{K_R}k(a-c)\\
&+\frac{2}{\pi R}(1-k)\left[\left(\delta_0-\frac{c^2}{2}\right)\arctan\sqrt{m^2-1}-\frac{1}{2}a\sqrt{c^2-a^2}\right]\\
&=\frac{w}{\sigma_0}
\end{aligned}
\tag{30}
$$

2.4. Non-dimensionalization of the governing equations

Following the non-dimensional formulations by Maugis (1992), we define the dimensionless contact radius A, dimensionless outer radius of the cohesive zone C, dimensionless penetration Δ, dimensionless normal force $\overline{P}$, and the Maugis parameter λ, as follows

$$
A = \frac{a}{\left(\frac{\pi wR^2}{\chi}\right)^{1/3}},
\tag{31}
$$

$$
C = \frac{c}{\left(\frac{\pi wR^2}{\chi}\right)^{1/3}},
\tag{32}
$$

$$
\Delta = \frac{\delta}{\left(\frac{\pi^2 w^2 R}{\chi^2}\right)^{1/3}},
\tag{33}
$$

$$
\overline{P} = \frac{P}{\pi wR},
\tag{34}
$$

$$
\lambda = \frac{2\sigma_0}{\left(\frac{\pi w\chi^2}{R}\right)^{1/3}},
\tag{35}
$$

where $\chi = 8K_R/3$. The first two governing equations can be written in a non-dimensional form as

$$
\Delta + (k-1)\Delta_0 = kA^2 - \frac{4}{3}k\lambda A\sqrt{m^2-1},
\tag{36}
$$

$$
\overline{P} = \frac{3A}{2k}[\Delta + (k-1)\Delta_0] - \frac{1}{2}A^3 - \lambda A^2\left(m^2\arctan\sqrt{m^2-1}-\sqrt{m^2-1}\right).
\tag{37}
$$

The third governing equation in the Stage-I ($C \ge A_0$) becomes

$$\frac{\lambda A^2}{2}\left[\sqrt{m^2-1}+(m^2-2)\arctan\sqrt{m^2-1}\right]-\lambda(\Delta-A^2)\arctan\sqrt{m^2-1}+\frac{4}{3}\lambda^2 k(A-C)$$
$$+\lambda(1-k)\left[\left(\Delta_0-\frac{C^2}{2}\right)\left(\arcsin\frac{A_0}{C}-\arcsin\frac{A}{C}\right)+\frac{1}{2}A_0\sqrt{C^2-A_0^2}-\frac{1}{2}A\sqrt{C^2-A^2}\right]$$
$$+\frac{4}{3}\lambda^2(k-1)C_0\left[\text{EllipticE}\left(\frac{\pi}{2},\frac{C^2}{C_0^2}\right)-\text{EllipticE}\left(\arcsin\frac{A_0}{C},\frac{C^2}{C_0^2}\right)\right]$$
$$=1$$

$$(38)$$

While, in the Stage-II ($C \leq A_0$), it becomes

$$\frac{\lambda A^2}{2}\left[\sqrt{m^2-1}+(m^2-2)\arctan\sqrt{m^2-1}\right]-\lambda(\Delta-A^2)\arctan\sqrt{m^2-1}+\frac{4}{3}\lambda^2 k(A-C)$$
$$+\lambda(1-k)\left[\left(\Delta_0-\frac{C^2}{2}\right)\arctan\sqrt{m^2-1}-\frac{1}{2}A\sqrt{C^2-A^2}\right]$$
$$=1$$

$$(39)$$

The above governing equations can be solved numerically through the computational procedure explained in Appendix B.

3. Results

In contrast to the elastic system, whose response is solely governed by the Maugis parameter λ, the behavior of the viscoelastic system is further affected by the ratio of the relaxed to instantaneous moduli, k, and the initial contact conditions, such as a_0 and δ_0. It is noted that, for the initial relaxed state, δ_0 is correlated to a_0 through the elastic Maugis-Dugdale model. In order to explore the influences of these three parameters and to identify possible mechanisms for the apparent adhesion enhancement (if there are any), the detachment behaviors of the viscoelastic systems will be first presented in two typical regimes in this section. A more general discussion will be followed in a later section. Specifically, in this section, we will calculate the unloading curves from different initial contact conditions for systems with either a very large λ value (the JKR-like regime) or a very small λ value (the DMT-like regime). In our calculations, the ratio of the relaxed to instantaneous moduli is kept at $k = 0.05$, unless otherwise specified.

3.1. JKR-like regime

To explore the behavior in the JKR-like regime, we calculated the responses for a system with the Maugis parameter of $\lambda = 100$. It is noted that the Maugis parameter defined in Eq. (35) is based on the relaxed modulus. Fig. 3 (a) and (b) are the calculated unloading curves of $\bar{P} \sim A$ and $\bar{P} \sim \Delta$, where the different colors represent the responses with different initial contact radii $A_0 = [1,2,3,4,5]$. It is noted that the unloading curves in the figure depict the process from the initial contact state all the way to the point of interfacial instability under displacement control condition (i.e., when the governing equations no longer have real solutions). In each calculated curve, the Stage-I response is represented by a solid-line segment, while Stage-II response is shown by a dashed-line segment. For better comparison, we also included the elastic Maugis-Dugdale solution in the figures.

From the unloading curves, one can clearly see that the detachment process depends on the initial contact conditions. To illustrate
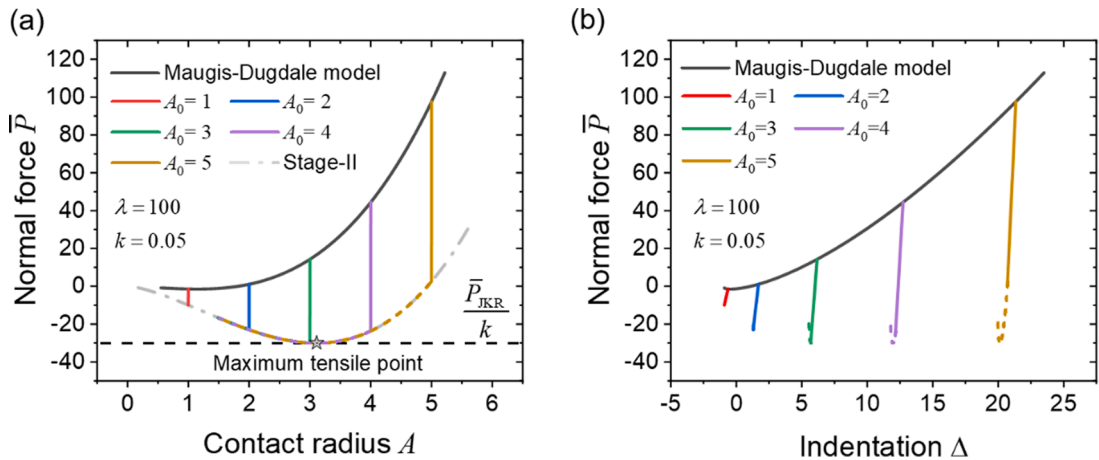

Fig. 3. (a) Variation of $\bar{P}$ with A, and (b) variation of $\bar{P}$ with Δ for different values of initial contact radius in the JKR-like regime ($\lambda = 100$). The solid and dashed lines represent the responses in Stage-I and Stage-II, respectively, while the dash-dot curve in (a) indicates the Stage-II master curve.

the response of the system during the detachment process, we will first focus on cases where the initial contact radius is relatively large (say $A_0 > 3$). Taking the case of $A_0 = 4$ as an example, one can see that the detachment process involves two stages. In Stage-I, when the detachment initiates, the normal force decreases rapidly compared with the elastic case. The pronounced decrease can be attributed to the unloading of the Hertzian contact zone according to the instantaneous modulus. As the detachment proceeds, C reduces to be less than A_0 and the system enters Stage-II, where A continues to decrease until the interface becomes unstable and fully detached under displacement control. During this process, the normal force $\overline{P}$ initially decreases, reaching a maximum negative (tensile) value $\overline{P}_{\min}$, and then its absolute value decreases again until Δ reaches the minimum value. It is noted that the maximum tensile force may occur while the indentation depth remains positive. This unique behavior can be understood as follows: When the indenter is rapidly retracted, the viscoelastic substrate does not have sufficient time to fully recover from its initial deformation. As the deformation of the substrate lags behind the indenter's motion during its rapid retraction, the interface starts to separate, leading to enhanced adhesion even while the overall indentation depth is still positive. The magnitude of the maximum tensile force, $|\overline{P}_{\min}|$, is defined as the pull-off force. According to Fig. 3 (a), we notice that the unloading curves $\overline{P} \sim A$ with different A_0 all converge to a single curve as the system enters Stage-II. Such behavior is not unexpected and can be explained as follows. By substituting Eq. (36) into Eqs. (37) and (39) and simplifying the expressions, we can get

$$\overline{P} = A^3 - \lambda A^2 \left(\sqrt{m^2 - 1} + m^2 \arctan \sqrt{m^2 - 1} \right) \tag{40}$$

and

$$k \frac{\lambda A^2}{2} \left[\sqrt{m^2 - 1} + (m^2 - 2) \arctan \sqrt{m^2 - 1} \right] + k \frac{4\lambda^2 A}{3} \left(\sqrt{m^2 - 1} \cdot \arctan \sqrt{m^2 - 1} - m + 1 \right) = 1 \cdot \tag{41}$$

Therefore, once the system enters Stage-II, the unloading curve $\overline{P} \sim A$ is fully determined by Eqs. (40) and (41), which are both independent of the initial contact conditions. This Stage-II master curve is shown as the dash-dot curve in Fig. 3 (a). By examining the Stage-II master unloading curve, we observe that the pull-off force under rapid loading will be enhanced by a factor up to $(1/k)$ compared with the elastic case (see the maximum tensile point marked by a star). Here, the maximum adhesion amplification factor $(1/k)$ can only be achieved when the initial contact radius is large than a critical value A_c (in the example case here, $A_c = 3.11$). If the initial contact radius is relatively small, e.g. $A_0 = 2$, the corresponding unloading curve in Stage-II will not pass through the maximum tensile point. As a result, the adhesion amplification will be reduced and will depend on the specific value of the initial contact radius. If the contact radius is even smaller, e.g. $A_0 = 1$, the system will become unstable at the end of Stage-I without entering Stage-II. In this case, the pull-off force will also depend on the specific value of the initial contact radius.

To explore the amplification mechanism, we took $A_0 = 4$ as an example again and analyzed the variations of the contact and cohesive zones at different moments during the detachment process. As shown in Fig. 4 (a), as the detachment progresses, both A and C decrease monotonically, but the normalized area of the annular cohesive zone, $\pi(C^2 - A^2)$, increases notably, especially during Stage-I. To better visualize this effect, we plotted the profiles of the sphere and the substrate at both the initial moment and the pull-off moment in Fig. 4 (b) and (c). One can see that the size of the cohesive zone at the moment of pull-off under a rapid loading is substantially larger than its initial state. This increase in the cohesive zone can also be understood from the fracture mechanics point of view. It is known that the size of the process zone near a crack tip is proportional to the square of the critical value of stress intensity factor K_{Ic}^2, which in turn is proportional to the elastic modulus of the material (Ciavarella et al., 2021; Greenwood and Johnson, 1981). For the interfacial crack formed during the detachment process, the effective modulus of the substrate at high speeds becomes $(1/k)$
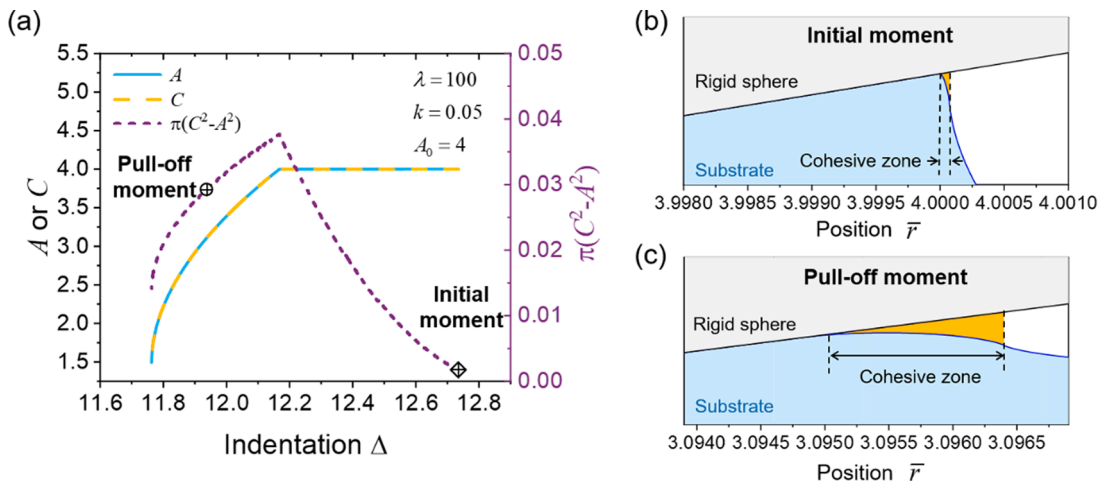

Fig. 4. (a) Variations of the contact radius A, outer radius of the cohesive zone radius C, and the normalized cohesive zone area with indentation Δ, in the case of $A_0 = 4$. (b) Interface profile at the initial moment. (c) Interface profile at the pull-off moment.

times the relaxed value, thus the size of the cohesive zone is amplified accordingly.

3.2. DMT-like regime

For the DMT-like regime, we also calculated the unloading curves $\overline{P} \sim A$ and $\overline{P} \sim \Delta$ for a system with the Maugis parameter $\lambda = 0.01$ using different initial contact radii. To better illustrate the system responses, we will discuss the results under two scenarios. The first scenario involves cases with relatively small initial contact radii, where the entire detachment process is restricted to Stage-I. The second scenario involves cases with relatively large initial contact radii, where the detachment process includes both Stage-I and Stage-II.

For the first scenario, we calculated the unloading curves $\overline{P} \sim A$ and $\overline{P} \sim \Delta$ for systems with relatively small initial contact radii, *i.e.* $A_0 = [1, 2, 3, 4, 5]$ and plotted them in Fig. 5 (a) and (b). In contrast to the JKR-like regime, the $\overline{P} \sim A$ curves in the DMT-like regime closely follow the elastic solution, and the enhancement of the pull-off force remains mild when the initial contact radius varies from 1 to 5. However, because the contact zone still unloads with the instantaneous modulus, the normal load drops rapidly upon retraction of the indenter sphere, as shown in Fig. 5 (b).

To better understand the system responses shown in Fig. 5 (a), (b), we took the case of $A_0 = 4$ as an example and plotted the variations of A and C during the detachment process. As shown in Fig. 6 (a), the initial outer radius of the cohesive zone C_0 is significantly larger than the contact radius A_0, which is a typical feature of the DMT-like contacts. Upon retraction of the sphere, the contact radius A rapidly decreases due to unloading of the contact zone with the instantaneous modulus. However, the outer radius of the cohesive zone C and the cohesive zone area $\pi(C^2 - A^2)$ remain nearly constant, even when A is reduced to zero. This process is better visualized when the profiles of the interface at the initial moment and the pull-off moment are plotted in Fig. 6 (b) and (c). The insignificant change in the cohesive zone area essentially explains why the $\overline{P} \sim A$ curves are close to the elastic solution. For this scenario, because C barely changes during the detachment process, the pull-off force can be approximated by $|P_{\min}| \approx \pi\sigma_0 c_0^2$, or $|\overline{P}_{\min}| \approx \frac{1}{2}\pi\lambda C_0^2$ in the non-dimensional form. For the DMT-like contacts, the initial outer radius of the cohesive zone can be determined as $C_0 = \sqrt{4/(\pi\lambda) + 2A_0^2}$ (detailed derivations are provided in Appendix C). Therefore, the pull-off force can be estimated as $|\overline{P}_{\min}| = 2 + \pi\lambda A_0^2$. This expression suggests that, as long as the system has a finite initial contact radius, *i.e.* $A_0 \geq 0$, the normalized pull-off force would be enhanced by an amount of $\pi\lambda A_0^2$. However, because λ is small for the DMT-like contacts, the enhancement is minimal if the initial contact radius is not too large. Previous literature has demonstrated that, in the limit of long-range adhesion (*i.e.* the DMT-like regime), the unloading rate has little effect on the pull-off force. Our model clarifies the underlying mechanism for this phenomenon (Ciavarella, 2022; Violano and Afferrante, 2022a).

If the initial contact radius is sufficiently large, the detachment process in the DMT-like regime can also progress Stage-II. Based our calculations, we found that for the system with $\lambda = 0.01$ and $k = 0.05$, the critical initial contact radius is approximately $A_c \approx 50$. To illustrate the system responses for this second scenario, we plotted the unloading curves $\overline{P} \sim A$ and $\overline{P} \sim \Delta$ with the initial contact radius $A_0 = [60, 70, 80]$ and showed them in Fig. 7 (a) and (b). Because of the large initial contact radius, the magnitude of the normal load has a very large range in Fig. 7 (a) and (b). To better illustrate the differences among the curves and the transition behavior, we included two zoom-in plots in the insets of Fig. 7 (a) at $A \sim 50$ and at $A \sim 0$. Similar to the JKR-like regime, once the system enters Stage-II all the unloading $\overline{P} \sim A$ curves converge to a master curve, which gives a pull-off force of $\overline{P}_{\text{DMT}}/k$ with an amplification factor of $(1/k)$.

To understand the mechanism of the adhesion enhancement in this scenario, we again plotted the variation of A and C during the detachment process for the case of $A_0 = 70$ in Fig. 8 (a). One can see that the detachment process indeed goes through two stages. In Stage-I ($C \geq A_0$), C reduces slowly but A decreases rapidly. In Stage-II ($C \leq A_0$), both C and A noticeably decrease, but the reduction
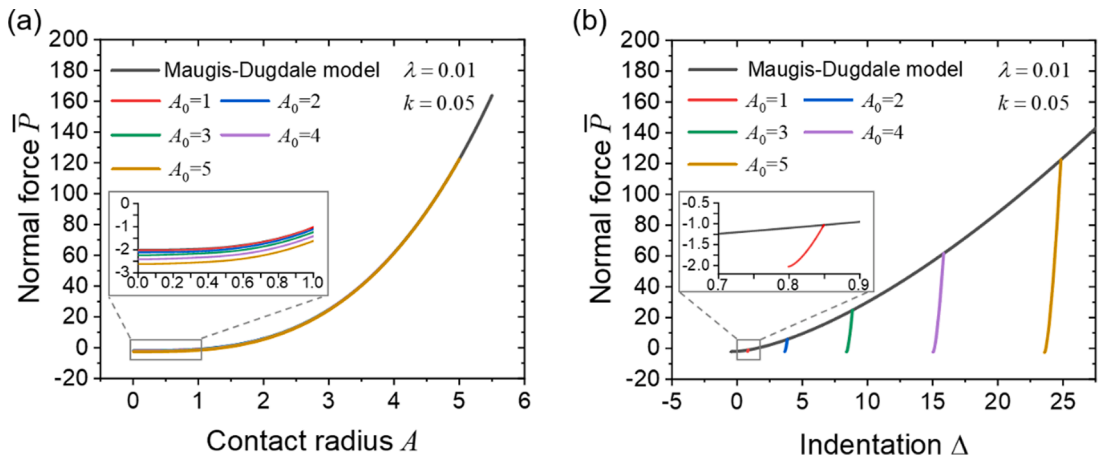

Fig. 5. (a) Variation of $\overline{P}$ with A, and (b) variation of $\overline{P}$ with Δ for relatively small values of initial contact radius, $A_0 = [1, 2, 3, 4, 5]$, in the DMT-like regime ($\lambda = 0.01$). The solid and dashed lines represent the responses in Stage-I and Stage-II, respectively.
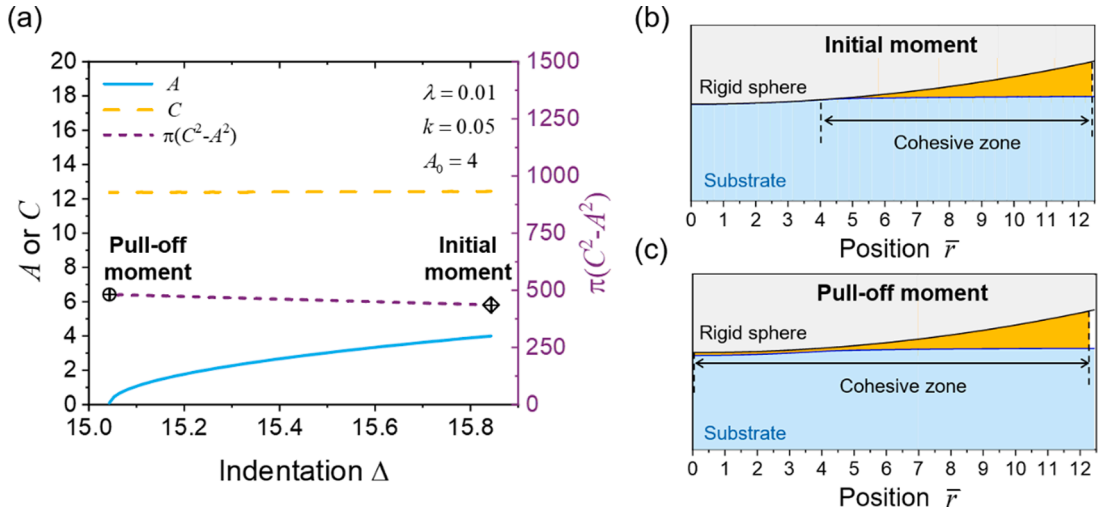
Fig. 6. (a) Variations of contact radius A, the outer radius of the cohesive zone radius C, and the normalized cohesive zone area with indentation Δ in the case of $A_0 = 4$. (b) Interface profile at the initial moment. (c) Interface profile at the pull-off moment.

speed of A is still much larger than C. By comparing the interface profiles at the initial moment and the pull-off moment in Fig. 8 (b) and (c), one can see that the enlarged cohesive zone area at the moment of pull-off is due to the crater shape of the substrate. The concave surface of the substrate increases the effective radius of curvature of the contact, thereby enhancing adhesion. By considering the viscoelastic deformation of the substrate at the moment of pull-off, we can calculate the effective radius of curvature between the sphere and the substrate, which turns out to be R/k (detailed derivations are provided in Appendix D). The enlarged radius of curvature will enhance the pull-off by a factor of $(1/k)$, which is consistent with our model prediction.

4. Discussions and validations

4.1. Influences of the Maugis parameter and the initial contact state

As revealed in Section 2, the system response during the detachment process depends on both the Maugis parameter and the initial contact state. To quantify the effects of these two parameters on the apparent adhesion enhancement, we calculated the pull-off forces for a viscoelastic system with $k = 0.05$ while systematically varying the Maugis parameter (from 0.001 to 100) under different initial contact radii. As shown in Fig. 9 (a), if the initial contact radius is sufficiently large (e.g. $A_0 = 200$), the pull-off force will always be amplified by a factor of $(1/k)$ regardless of the Maugis parameter. In other words, the normalized pull-off force will change gradually from $\bar{P}_{JKR}/k$ to $\bar{P}_{DMT}/k$ as the system transit from the JKR-like regime to the DMT-like regime. However, if the initial contact radius is not sufficiently large, then the enhancement of the pull-off force may be limited, with its magnitude determined both by the Maugis
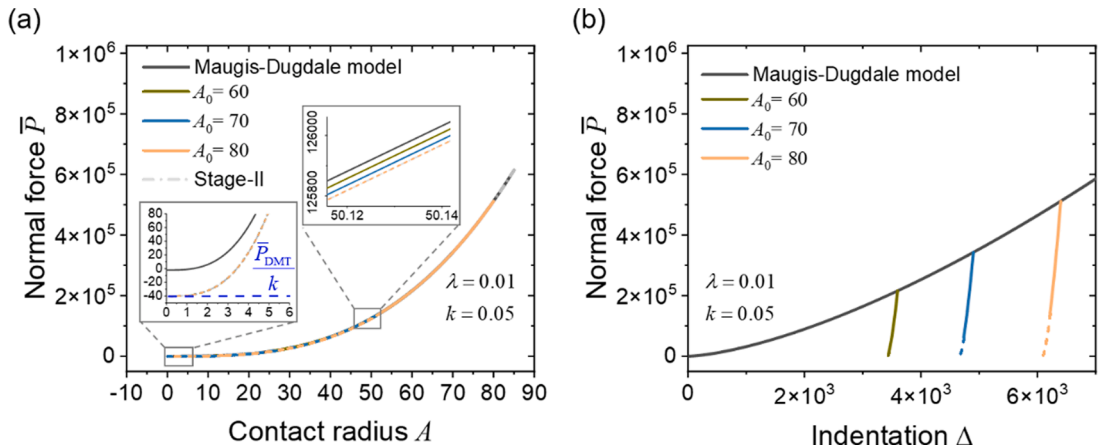

Fig. 7. (a) Variation of $\bar{P}$ with A, and (b) variation of $\bar{P}$ with Δ for different values of the initial contact radius, $A_0 = [60, 70, 80]$, in the DMT-like regime ($\lambda = 0.01$). The solid and dashed lines represent the responses in Stage-I and Stage-II, respectively, while the dash-dot curve in (a) indicates the Stage-II master curve.
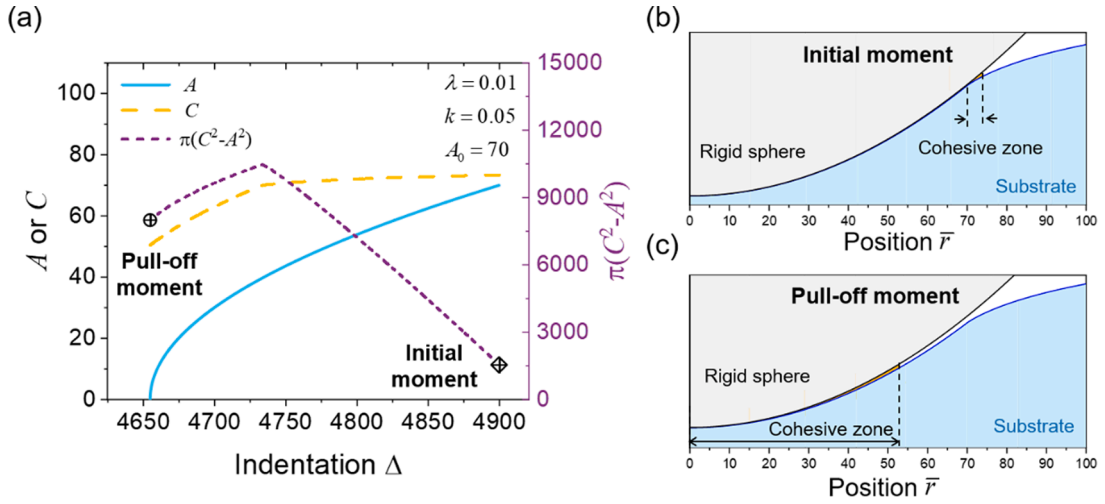
Fig. 8. (a) Variations of contact radius A, outer radius of the cohesive zone radius C, and the normalized cohesive zone area with indentation Δ in the case of $A_0 = 70$. (b) Interface profile at the initial moment. (c) Interface profile at the pull-off moment.
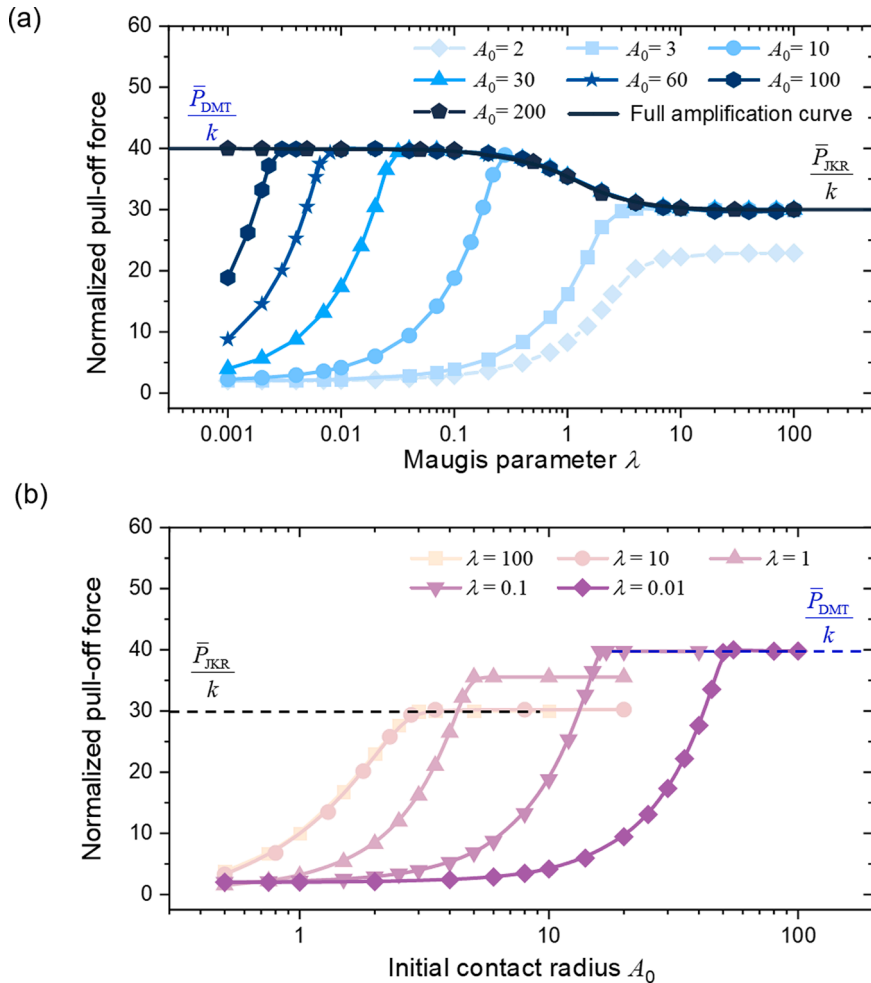

Fig. 9. (a) Variation of pull-off force with λ for different A_0 ($k = 0.05$). (b) Variation of pull-off force with A_0 for different λ ($k = 0.05$).

parameter and the initial contact radius. As can be seen in Fig. 9 (a), for a fixed and finite initial contact radius, the adhesion enhancement is generally low when λ is small (*i.e.* in the DMT-like regime) and it gradually increases to the full amplification level as λ becomes larger. Therefore, one is more likely to observe an apparent adhesion enhancement for a JKR-like contact than for a DMT-like contact given a same initial contact radius.

We also plotted the pull-off force as a function of the initial contact radius for systems with different Maugis parameters. As shown in Fig. 9 (b), for a given Maugis parameter, the apparent adhesion enhancement is low when A_0 is small and the enhancement becomes higher as A_0 increases. When the initial contact radius exceeds a certain critical value, A_c, the apparent adhesion enhancement will reach the aforementioned full amplification level. Similar dependence of adhesion on the initial contact state has been observed in biological systems (Jiao et al., 2000), though it was attributed to the hysteresis of the adhesive interactions (Schargott et al., 2006). Based on the results shown in Fig. 9 (b), one can see that the critical initial contact radius A_c depends on the Maugis parameter. Generally, A_c is larger when λ is smaller, *i.e.* a larger initial contact radius is needed for more DMT-like contacts. To quantify the dependence of A_c on λ, we plotted the variation of the critical initial contact radius A_c with λ in Fig. 10. By fitting the data, we found that

$$A_c = 3.21 \cdot \lambda^{-0.59} + 3.11 \qquad (42)$$

gives a good approximation of A_c when λ is given. From Fig. 10 and Eq. (42), one can see that when λ approaches infinity (the JKR-like regime), the critical value A_c converges to a constant, approximately 3.11. However, as λ approaches zero (the DMT-like regime), the critical value increases rapidly with a scaling law of $\lambda^{-0.59}$. It should be noted that the fitting expression given in Eq. (43) is based on the system with $k = 0.05$. For systems with different k values, the dependence remains qualitatively similar but with different pre-factor and power index. A more detailed discussion on the influence of k can be found in Appendix E.

While a large initial normalized contact radius is required to achieve significant adhesion enhancement in the DMT-like regime, this does not necessarily correspond to a large absolute value of the initial contact radius. As the normalized contact radius is defined as $A = a / \left(\pi w R^2 / \chi\right)^{1/3}$, if the normalization factor $\left(\pi w R^2 / \chi\right)^{1/3}$ is small enough, a relatively small contact radius may also lead to a significant normalized contact radius. However, since we have adopted the Hertzian solution as well as the parabolic approximation for the contact shape of the spherical indenter in our model, the contact radius should be much smaller than the radius of indenter, i.e. $a \ll R$, which requires that $A \ll (\chi R / \pi w)^{1/3}$.

The results shown in Fig. 11 provide a more comprehensive view of the impacts of the Maugis parameter and the initial contact state on the apparent adhesion enhancement. This insight can aid in better interpreting model predictions found in the existing literature. For example, the Das-Chasiotis model (Das and Chasiotis, 2021) suggests that the apparent adhesion enhancement is independent of the Maugis parameter and the pull-off force would be enhanced by a factor of $(1/k)$ as long as the loading rate is sufficiently high. However, the Ciavarella model (Ciavarella, 2022) reveals that the apparent adhesion enhancement at high speeds only occurs in the JKR-like regime but not in the DMT-like regime. Although the predictions from these two models may appear contradicting, they are both conditionally correct, as shown in Fig. 11. Based on our model calculations, if the initial contact radius is sufficiently large, then the pull-off force would indeed always be enhanced by a factor of $(1/k)$, regardless of the Maugis parameter. Under this condition, the Das-Chasiotis model is correct. However, as described by Eq. (42), to reach the full adhesion amplification level, the initial contact radius of the DMT-like contacts ($\lambda \to 0$) would be very high or even practically impossible. In this context, the prediction of the Ciavarella model is also correct when the system has a relatively small initial contact radius. Although the prediction of the Ciavarella model is qualitatively consistent with the new model presented here, we noticed that the transition behavior is slightly different. As shown in Fig. 11, the full adhesion amplification predicted by the Ciavarella model only occurs at relatively large values of λ. In contrast, our new model suggests the full adhesion amplification can occur at much smaller λ values. This discrepancy
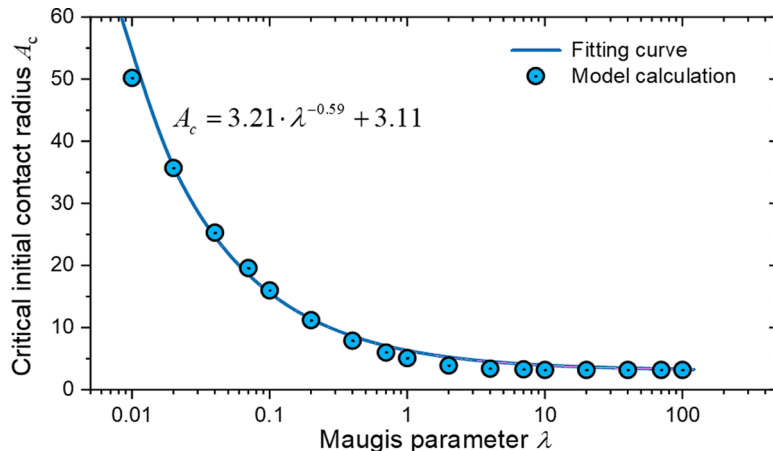

Fig. 10. Variation of the critical initial contact radius A_c with λ ($k = 0.05$).
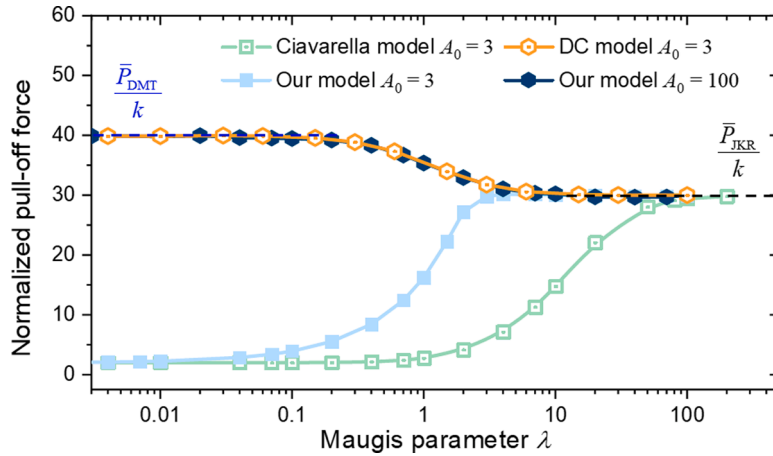
Fig. 11. Variations of the pull-off force with the Maugis parameter λ predicted by different models.

arises from the fact that the Ciavarella model neglects the viscoelasticity of the Hertzian region, whereas our new model includes the viscoelastic effect both in the Hertzian part and in the cohesive zone.

Regarding the mechanisms for the adhesion amplification, two sources have been identified in Section 3: One from the viscoelastic effect around the cohesive zone, and the other from the viscoelastic effect within the Hertzian contact zone. Our findings are qualitatively consistent with the recent work by Mandriota and coworkers (Mandriota et al., 2024). Here, it is also worth pointing out that, although these two mechanisms seem different, they both originate from the viscoelastic stiffening effect of the substrate material. In the more general transition region, both of them would contribute to the enlargement of the cohesive zone area. During the propagation process of the interfacial crack, the substrate material initially within the Hertzian contact zone has to enter the cohesive zone, making it physically challenging to separate one mechanism from the other.

4.2. Validation by boundary element method (BEM) simulations

To validate our theoretical model, we conducted boundary element method (BEM) simulations for similar viscoelastic contact problem and compared the calculated pull-off force for systems with different Maugis parameters and initial contact radii. As shown in Fig. 12, a rigid sphere is first brought into contact with a viscoelastic substrate quasi-statically and then pulled away from the substrate under a speed v. To mimic the high speed behavior, we gradually increased the retraction speed until the simulation results converged to the "infinite speed" limit. Numerically, we found that $\bar{v} = v\tau_0/h_0 = 10 \times 2^{12}$ is large enough to approximate the "infinite speed" limit behavior, where τ_0 is the characteristic time of the viscoelastic substrate. Further increase in the retraction rate did not affect the results within the limits of numeric accuracy. In this way, the simulations can be regarded as fast loading, consistent with the assumption of our upper bound theoretical model. The interaction between the sphere and the substrate is assumed to be governed by the Lennard-Jones traction-separation law (Greenwood, 1997)

$$\sigma(h) = \frac{8w}{3h_0}\left[\left(\frac{h_0}{h}\right)^3 - \left(\frac{h_0}{h}\right)^9\right], \tag{43}$$

where σ is the interfacial stress (positive represents tensile), h is the local gap, h_0 is the equilibrium distance, and w is the work of adhesion. The implementation of the BEM simulations was based on a numerical scheme proposed in the literature (Papangelo and Ciavarella, 2020, 2023). Because the Lennard-Jones law used in BEM model is different from the Dugdale cohesive zone law used in the theoretical model, to rationally compare their results, we adopted the following correlation $\lambda = 0.6628\mu$ as proposed by Zheng and Yu (2007). Here, λ is the Maugis parameter from the theoretical model as defined in Eq. (35); while μ is the Tabor parameter from the BEM model, defined as $\mu = \left[Rw^2/\left(E_R^{*2}h_0^3\right)\right]^{1/3}$.

Fig. 13 shows the variations of the normalized pull-off force as a function of the initial contact radius A_0 for different Tabor parameters $\mu = [0.1, 0.57, 3.24]$ and $k = 0.05$ calculated by the BEM model. To best compare the results, the contact radius used in Fig. 13 is determined by taking the radial coordinate where the tensile stress reaches its peak (Greenwood, 1997). Similar to the results shown in Fig. 9 (b), one can see that, for any fixed Tabor parameters, as long as the initial contact radius is larger than the critical value, the pull-off force will be enhanced by a factor of $(1/k)$. Considering the shape difference of the two cohesive zone models, the reasonable agreement between the theory and the BEM simulations offers a good validation of the new theoretical model.

5. Conclusion

In this work, we revisit the viscoelastic adhesive contact problem, where an indenter initially adhered to a fully relaxed viscoelastic
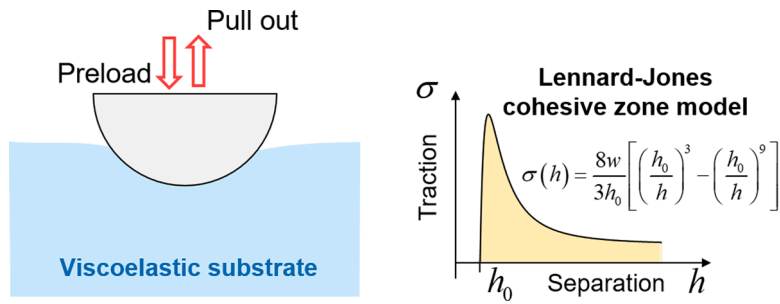
Fig. 12. A schematic diagram showing the model used in the BEM simulations.

substrate is retracted at an infinitely high speed. Based on Barthel's framework and the Dugdale-type cohesive model, a set of governing equations have been derived to describe the full detachment behavior. Our theoretical model confirms that the apparent adhesion enhancement is generally affected by both the Maugis parameter and the initial contact state. More specifically, the pull-off force will be enhanced by a constant factor of $(1/k)$ regardless of the Maugis parameter if the initial contact radius exceeds a critical value A_c. However, if the initial contact radius is smaller than A_c, the apparent adhesion enhancement will be limited, showing dependence on the Maugis parameter and the preload condition. Our model calculations also provide an empirical expression of this critical initial contact radius A_c, whose value converges to a constant in the JKR-like regime but diverges rapidly with an inverse power law as the Maugis parameter approaches zero. This mathematical feature of A_c resolves the seemingly contradicting results in the literature and explains why the apparent adhesion enhancement is less observed in the DMT-like regime than in the JKR-like regime. In addition, this work identifies two mechanisms for the adhesion amplification. In the JKR-like regime, the pull-off force is enhanced at high speeds due to the viscoelastic stiffening effect of the substrate material around the cohesive zone. In the DMT-like regime, the adhesion enhancement is caused by the retarded deformation within the Hertzian contact zone due to the viscoelastic effect. Although these two mechanisms seem somewhat different, both of them lead to the same result, *i.e.* enlargement of the cohesive zone area. In the more general transition regime, both of these two mechanisms will naturally get involved during the detachment process. Physically, it is hard to separate one mechanism from the other, because the substrate material originally residing within the Hertzian contact zone has to enter the cohesive zone during propagation of the interfacial crack.

CRediT authorship contribution statement

Qingao Wang: Writing – review & editing, Writing – original draft, Visualization, Validation, Investigation, Formal analysis. **Antonio Papangelo:** Writing – review & editing, Validation, Investigation, Funding acquisition. **Michele Ciavarella:** Writing – review & editing, Investigation. **Huajian Gao:** Writing – review & editing, Investigation. **Qunyang Li:** Writing – review & editing, Writing – original draft, Visualization, Validation, Supervision, Resources, Project administration, Investigation, Funding acquisition, Formal analysis, Conceptualization.
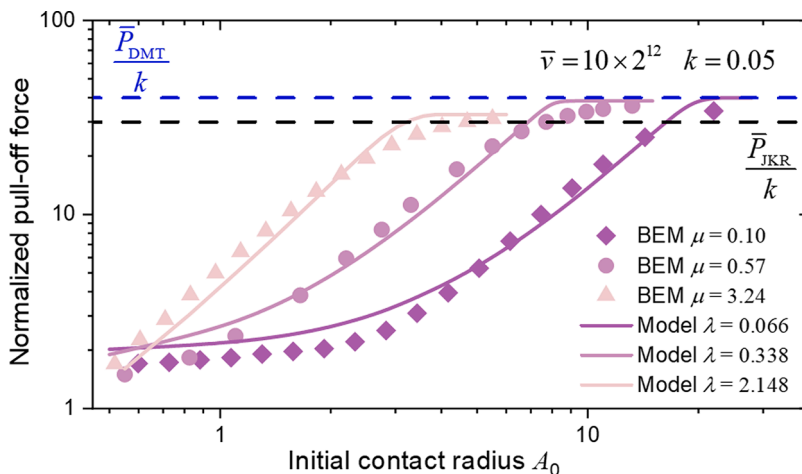

Fig. 13. Comparison between the BEM simulations and the theoretical model predictions.

Declaration of competing interest

Acknowledgement

Appendix A. Derivation of Eq. (29)

The integral of Eq. (25) can be further divided into two parts, i.e. from a to a_0 and from a_0 to c. Therefore, it can be rewritten as

$$
\begin{aligned}
h(c) = \frac{2}{\pi R}\left[\frac{a}{2}\sqrt{c^2-a^2}+\left(\frac{c^2}{2}-a^2\right)\arctan\sqrt{m^2-1}\right]-\frac{2}{\pi}\left(\delta-\frac{a^2}{R}\right)\arctan\sqrt{m^2-1}\\
+\frac{2}{\pi}\int_a^{a_0}ds\cdot\frac{\theta(s)}{\sqrt{c^2-s^2}}+\frac{2}{\pi}\int_{a_0}^{c}ds\cdot\frac{\theta(s)}{\sqrt{c^2-s^2}}
\end{aligned}
\tag{A.1}
$$

In the region a to a_0, following Eq. (28), we have

$$
\begin{aligned}
\theta(s) &= \frac{k}{K_R}g(s)+(1-k)\theta_0(s)\\
&= -\frac{k}{K_R}\sigma_0\sqrt{c^2-s^2}+(1-k)\left(\delta_0-\frac{s^2}{R}\right) .
\end{aligned}
\tag{A.2}
$$

In the region a_0 to c, following Eq. (27), we have

$$
\begin{aligned}
\theta(s) &= \frac{k}{K_R}g(s)+\frac{1-k}{K_R}g_0(s)\\
&= -\frac{k}{K_R}\sigma_0\sqrt{c^2-s^2}-\frac{1-k}{K_R}\sigma_0\sqrt{c_0^2-s^2} .
\end{aligned}
\tag{A.3}
$$

Substituting Eqs. (A.2) and (A.3) into Eq. (A.1), we obtain

$$
\begin{aligned}
h(c) = \frac{2}{\pi R}\left[\frac{a}{2}\sqrt{c^2-a^2}+\left(\frac{c^2}{2}-a^2\right)\arctan\sqrt{m^2-1}\right]-\frac{2}{\pi}\left(\delta-\frac{a^2}{R}\right)\arctan\sqrt{m^2-1}+\frac{2}{\pi}\frac{\sigma_0}{K_R}k(a-c)\\
+\frac{2}{\pi R}(1-k)\left[\left(\delta_0-\frac{c^2}{2}\right)\left(\arcsin\frac{a_0}{c}-\arcsin\frac{a}{c}\right)\right]+\frac{2}{\pi R}(1-k)\left(\frac{1}{2}a_0\sqrt{c^2-a_0^2}-\frac{1}{2}a\sqrt{c^2-a^2}\right)\\
+\frac{2}{\pi}\frac{\sigma_0}{K_R}(k-1)c_0\left[\text{EllipticE}\left(\frac{\pi}{2},\frac{c^2}{c_0^2}\right)-\text{EllipticE}\left(\arcsin\frac{a_0}{c},\frac{c^2}{c_0^2}\right)\right]
\end{aligned}
\tag{A.4}
$$

where $\text{EllipticE}(\alpha,p) = \int_0^{\alpha}dx\cdot\sqrt{1-p\sin^2 x}$ is the elliptic integral of the second kind.

Appendix B. Computational procedure to solve the governing equations

1. Input the initial contact radius, A_0, the Maugis parameter, λ, the ratio of relaxed to instantaneous moduli k, and the indentation increment $d\Delta$. Firstly, we calculate the corresponding initial indentation Δ_0, normal force $\overline{P}_0$ and cohesive zone radius C_0 using the Maugis-Dugdale model with relaxed modulus.

2. Update the indentation $\Delta_i = \Delta_{i-1} - d\Delta$ and substitute it into Stage-I governing equations Eqs. (36), (37) and (38).
3. If the governing equations have real solutions, update the contact radius, A_i, the cohesive zone radius, C_i, and the normal force $\overline{P}_i$. If the governing equation do not have real solutions, end the process.
4. If $C_i \geq A_0$, return to step 2. If $C_i < A_0$, update the indentation, $\Delta_i = \Delta_{i-1} - d\Delta$ and substitute it into Stage-II governing equations Eqs. (36), (37) and (39) and return to step 3.

Appendix C. Estimation of C_0 in the DMT-like regime

At the initial moment, the substrate is in fully relaxed state. The initial contact radius A_0 and outer radius of cohesive zone C_0 satisfy the elastic Maugis-Dugdale model as

$$\frac{\lambda A_0^2}{2}\left[\sqrt{m_0^2 - 1} + (m_0^2 - 2)\arctan\sqrt{m_0^2 - 1}\right] + \frac{4\lambda^2 A_0}{3}\left(\sqrt{m_0^2 - 1} \cdot \arctan\sqrt{m_0^2 - 1} - m_0^2 + 1\right) = 1, \tag{C.1}$$

Where $m_0 = C_0/A_0$. Considering that $\lambda \to 0$ and $m_0 \to \infty$ for the DMT-like contacts, the second term on the left side of the equation is a higher-order small quantity compared with the first term, thus the Eq. (C.1) can be reduced to

$$\frac{\lambda A_0^2}{2}\left[\sqrt{m_0^2 - 1} + (m_0^2 - 2)\arctan\sqrt{m_0^2 - 1}\right] = 1. \tag{C.2}$$

Noticing that $(m_0^2 - 2) \gg \sqrt{m_0^2 - 1}$ and $\arctan\sqrt{m_0^2 - 1} \to \pi/2$, Eq. (C.2) can be simplified to

$$\frac{\pi\lambda}{4}\left(C_0^2 - 2A_0^2\right) = 1. \tag{C.3}$$

From Eq. (C.3), one can get $C_0 = \sqrt{4/(\pi\lambda) + 2A_0^2}$.

Appendix D. Effective contact radius at the pull-off moment in the DMT-like regime

At the initial moment, the viscoelastic substrate surface aligns with the spherical sphere. The surface displacement is

$$u_0(r) = \delta_0 - \frac{r^2}{2R}, \tag{D.1}$$

where δ_0 is the initial indentation, R is the radius of rigid sphere. And θ_0 can be obtained as $\theta_0(s) = \delta_0 - r^2/R$ from Eq. (6). As the rigid sphere is rapidly pulled away from the substrate, θ function can be obtained from Eq. (28) as

$$\theta(s) = (1-k)\theta_0(s). \tag{D.2}$$

Thus, the displacement of the substrate surface can be determined by

$$u(r) = \frac{2}{\pi}\int_0^r ds \cdot \frac{\theta(s)}{\sqrt{r^2 - s^2}}. \tag{D.3}$$

Substituting Eq. (D.2). into Eq. (D.3), we obtain the surface displacement at the pull-off moment

$$u(r) = (1-k)\left(\delta_0 - \frac{r^2}{2R}\right). \tag{D.4}$$

The radius of curvature of the substrate at $r = 0$ can be determined as

$$R_s = \left|\frac{(1 + u'^2)^{3/2}}{u''}\right| = \frac{1}{1-k}R. \tag{D.5}$$

Hence, the effective radius of curvature of the sphere-substrate system is

$$R_{\text{eff}} = \frac{1}{\frac{1}{R} - \frac{1}{R_s}} = \frac{R}{k}. \tag{D.6}$$

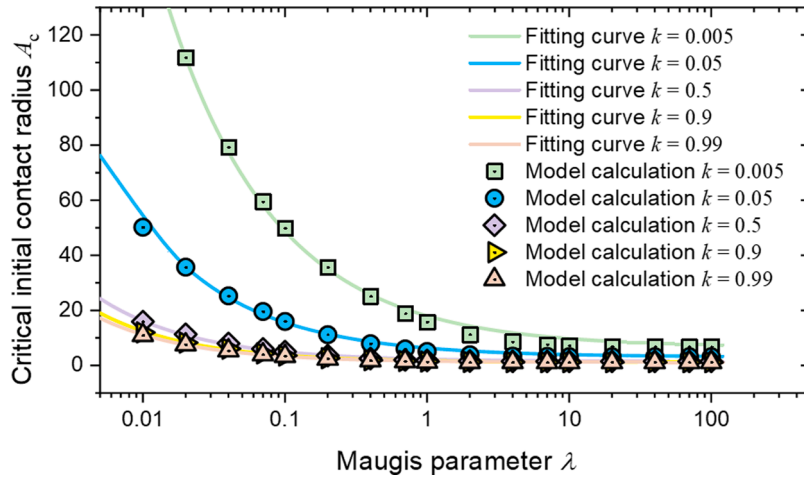## Appendix E. Influence of k on the critical initial contact radius under different Maugis parameters

Fig. E1. Variation of the critical initial contact radius A_c with λ for $k = [0.005, 0.05, 0.5, 0.9, 0.99]$.

We systematically varied the k value ($k = [0.005, 0.05, 0.5, 0.9, 0.99]$) and calculated the critical initial contact radius as a function of the Maugis parameter. The results are plotted in Fig. E1. By fitting the data for each value of k, we obtained the following empirical expressions:

$$A_c = \begin{cases} 11.31 \cdot \lambda^{-0.57} + 6.69, k = 0.005 \\ 3.21 \cdot \lambda^{-0.59} + 3.11, k = 0.05 \\ 0.81 \cdot \lambda^{-0.63} + 1.44, k = 0.5 \\ 0.54 \cdot \lambda^{-0.66} + 1.19, k = 0.9 \\ 0.46 \cdot \lambda^{-0.67} + 1.15, k = 0.99 \end{cases} \tag{E.1}$$

As indicated by Eq. (E.1), the absolute value of the power index increases with increasing k, while the pre-factor and the constant term decrease as k increases. Based on the definition of k, its value lies within the range of $0 < k < 1$. When $k \to 0$, the critical normalized initial contact radius A_c will tend to infinity in both the JKR-like and DMT-like regimes. When $k \to 1$, the system behaves as purely elastic. In such cases, the pull-off force is independent of the preload in the DMT-like regime, and thus the critical normalized initial contact radius will also approach infinity. In contrast, in the JKR-like regime, the pull-off force will be less than $P_{\text{JKR}} = 1.5\pi wR$ if the normalized initial contact radius is less than $A = \sqrt[3]{3/2}$. Therefore, the critical normalized initial contact radius will equal $A_c = \sqrt[3]{3/2}$ in the JKR-like regime when $k \to 1$.

Data availability

Data will be made available on request.

References

Afferrante, L., Violano, G., 2022. On the effective surface energy in viscoelastic Hertzian contacts. J. Mech. Phys. Solids 158.

Barthel, E., 2008. Adhesive elastic contacts: JKR and more. J. Phys. D-Appl. Phys. 41.

Barthel, E., Haiat, G., 2002. Approximate model for the adhesive contact of viscoelastic spheres. Langmuir 18, 9362–9370.

Chen, H., Feng, X., Huang, Y., Huang, Y.G., Rogers, J.A., 2013. Experiments and viscoelastic analysis of peel test with patterned strips for applications to transfer printing. J. Mech. Phys. Solids 61.

Ciavarella, M., 2021. Improved Muller approximate solution of the pull-off of a sphere from a viscoelastic substrate. J. Adhes. Sci. Technol. 35, 2175–2183.

Ciavarella, M., 2022. An upper bound for viscoelastic pull-off of a sphere with a Maugis-Dugdale model. J. Adhes. 98, 2118–2131.

Ciavarella, M., Cricri, G., McMeeking, R., 2021. A comparison of crack propagation theories in viscoelastic materials. Theor. Appl. Fract. Mec. 116.

Ciavarella, M., Wang, Q.-A., Li, Q., 2023. Maugis-Tabor parameter dependence of pull-off in viscoelastic line Hertzian contacts. J. Adhes. 99, 972–987.

Das, D., Chasiotis, I., 2021. Rate dependent adhesion of nanoscale polymer contacts. J. Mech. Phys. Solids 156.

de Gennes, P.-G., 1996. Soft adhesives. Langmuir 12, 4497–4500.

Derjaguin, B.V., Muller, V.M., Toporov, Y.P., 1975. Effect of contact deformations on the adhesion of particles. J. Colloid Interface Sci. 53, 314–326.

Feng, X., Meitl, M.A., Bowen, A.M., Huang, Y., Nuzzo, R.G., Rogers, J.A., 2007. Competing fracture in kinetically controlled transfer printing. Langmuir 23, 12555–12560.

Gent, A., Schultz, J., 1972. Effect of wetting liquids on the strength of adhesion of viscoelastic material. J. Adhes. 3, 281–294.

Greenwood, J., 2004. The theory of viscoelastic crack propagation and healing. J. Phys. D-Appl. Phys. 37, 2557.

Greenwood, J., Johnson, K., 1981. The mechanics of adhesion of viscoelastic solids. Philos. Mag. A 43, 697–711.

Greenwood, J.A., 1997. Adhesion of elastic spheres. Proc. R. Soc. A 453, 1277–1297.

Haiat, G., Huy, M.C.P., Barthel, E., 2003. The adhesive contact of viscoelastic spheres. J. Mech. Phys. Solids 51.

Hui, C.Y., Zhu, B.G., Long, R., 2022. Steady state crack growth in viscoelastic solids: A comparative study. J. Mech. Phys. Solids 159.

Jiang, L., Wu, M.J., Yu, Q.P., Shan, Y.X., Zhang, Y.Y., 2021. Investigations on the adhesive contact behaviors between a viscoelastic stamp and a transferred element in microtransfer printing. Coatings 11.

Jiao, Y., Gorb, S., Scherge, M., 2000. Adhesion measured on the attachment pads of Tettigonia viridissima (Orthoptera, Insecta). J. Exp. Biol. 203, 1887–1895.

Johnson, K., 1999. Contact mechanics and adhesion of viscoelastic spheres. In: ACS Symposium Series.

Johnson, K., Greenwood, J., 2002. Adhesion of viscoelastic spherical solids. In: Contact Mechanics: Proceedings of the 3rd Contact Mechanics International Symposium, Praia da Consolação, Peniche, Portugal, 17–21 June 2001. Springer, pp. 141–160.

Johnson, K., Kendall, K., Roberts, A., 1971. Surface energy and the contact of elastic solids. Proc. R. Soc. A 324, 301–313.

Kendall, K., 2001. Molecular adhesion and its applications: the sticky universe. Springer Science & Business Media.

Knauss, W.G., 1973. On the steady propagation of a crack in a viscoelastic sheet: Experiments and analysis, Deformation and fracture of high polymers. Springer, pp. 501–541.

Liang, C.M., Wang, F.J., Huo, Z.C., Shi, B.C., Tian, Y.L., Zhao, X.Y., Zhang, D.W., 2020. Pull-off force modeling and experimental study of PDMS stamp considering preload in micro transfer printing. Int. J. Solids Struct. 193, 134–140.

Lin, Y.Y., Hui, C.Y., 2002. Mechanics of contact and adhesion between viscoelastic spheres: An analysis of hysteresis during loading and unloading. J. Polym. Sci. Pt. B-Polym. Phys. 40, 772–793.

Lorenz, B., Krick, B.A., Mulakaluri, N., Smolyakova, M., Dieluweit, S., Sawyer, W.G., Persson, B.N.J., 2013. Adhesion: role of bulk viscoelasticity and surface roughness. J. Phys.-Condes. Matter 25.

Maghami, A., Tricarico, M., Ciavarella, M., Papangelo, A., 2024a. Viscoelastic amplification of the pull-off stress in the detachment of a rigid flat punch from an adhesive soft viscoelastic layer. Eng. Fract. Mech. 298.

Maghami, A., Wang, Q.A., Tricarico, M., Ciavarella, M., Li, Q.Y., Papangelo, A., 2024b. Bulk and fracture process zone contribution to the rate-dependent adhesion amplification in viscoelastic broad-band materials. J. Mech. Phys. Solids 193.

Mandriota, C., Menga, N., Carbone, G., 2024. Enhancement of adhesion strength in viscoelastic unsteady contacts. J. Mech. Phys. Solids 192.

Maugis, D., 1992. Adhesion of spheres: the JKR-DMT transition using a Dugdale model. J. Colloid Interface Sci. 150, 243–269.

Maugis, D., Barquins, M., 1978. Fracture mechanics and the adherence of viscoelastic bodies. J. Phys. D-Appl. Phys. 11, 1989.

Meitl, M.A., Zhu, Z.T., Kumar, V., Lee, K.J., Feng, X., Huang, Y.Y., Adesida, I., Nuzzo, R.G., Rogers, J.A., 2006. Transfer printing by kinetic control of adhesion to an elastomeric stamp. Nat. Mater. 5, 33–38.

Muller, V., 1999. On the theory of pull-off of a viscoelastic sphere from a flat surface. J. Adhes. Sci. Technol. 13, 999–1016.

Papangelo, A., Ciavarella, M., 2020. A numerical study on roughness-induced adhesion enhancement in a sphere with an axisymmetric sinusoidal waviness using Lennard-Jones interaction law. Lubricants 8.

Papangelo, A., Ciavarella, M., 2023. Detachment of a rigid flat punch from a viscoelastic material. Tribol. Lett. 71.

Peng, Z.L., Wang, C., Chen, L., Chen, S.H., 2014. Peeling behavior of a viscoelastic thin-film on a rigid substrate. Int. J. Solids Struct. 51, 4596–4603.

Persson, B., Brener, E., 2005. Crack propagation in viscoelastic solids. Phys. Rev. E 71, 036123.

Persson, B.N.J., 2021. On opening crack propagation in viscoelastic solids. Tribol. Lett. 69.

Petroli, A., Petroli, M., Romagnoli, M., Geoghegan, M., 2022. Determination of the rate-dependent adhesion of polydimethylsiloxane using an atomic force microscope. Polymer 262.

Schapery, R.A., 1975a. A theory of crack initiation and growth in viscoelastic media II. Approximate methods of analysis. Int. J. Fract. 11, 369–388.

Schapery, R.A., 1975b. A theory of crack initiation and growth in viscoelastic media: I. Theoretical development. Int. J. Fract. 11, 141–159.

Schapery, R.A., 1975c. A theory of crack initiation and growth in viscoelastic media: III. Analysis of continuous growth. Int. J. Fract. 11, 549–562.

Schargott, M., Popov, V., Gorb, S., 2006. Spring model of biological attachment pads. J. Theor. Biol. 243, 48–53.

Tabor, 1976. Surface force and surface interactions. J. Colloid Interface Sci. 58, 2–13.

Vandonselaar, K.R., Bellido-Aguilar, D.A., Safaripour, M., Kim, H., Watkins, J.J., Crosby, A.J., Webster, D.C., Croll, A.B., 2023. Silicone elastomers and the Persson-Brener adhesion model. J. Chem. Phys. 159.

Violano, G., Afferrante, L., 2022a. On the long and short-range adhesive interactions in viscoelastic contacts. Tribol. Lett. 70.

Violano, G., Afferrante, L., 2022b. Size effects in adhesive contacts of viscoelastic media. Eur. J. Mech. A-Solids 96.

Violano, G., Chateauminois, A., Afferrante, L., 2021a. A JKR-like solution for viscoelastic adhesive contacts. Front. Mech. Eng. 7, 664486.

Violano, G., Chateauminois, A., Afferrante, L., 2021b. Rate-dependent adhesion of viscoelastic contacts, Part I: Contact area and contact line velocity within model randomly rough surfaces. Mech. Mater. 160.

Violano, G., Chateauminois, A., Afferrante, L., 2021c. Rate-dependent adhesion of viscoelastic contacts. Part II: Numerical model and hysteresis dissipation. Mech. Mater. 158.

Wang, Z., Liu, X., 2024. Pull-off of viscoelastic spherical contact. J. Adhes. Sci. Technol. 1–19.

Williams, M.L., Landel, R.F., Ferry, J.D., 1955. The temperature dependence of relaxation mechanisms in amorphous polymers and other glass-forming liquids. J. Am. Chem. Soc. 77, 3701–3707.

Yin, H.B., Ma, Y.J., Feng, X., 2024. Rate-dependent peeling behavior of the viscoelastic film-substrate system. Int. J. Solids Struct. 286.

Zheng, Z., Yu, J., 2007. Using the Dugdale approximation to match a specific interaction in the adhesive contact of elastic objects. J. Colloid Interface Sci. 310, 27–34.